Journal of Alloys and Compounds 747 (2018) 166–175

Contents lists available at ScienceDirect

Journal of Alloys and Compounds

journal homepage: http://www.elsevier.com/locate/jalcom

Nanomaterials produced by laser beam ablating Sn-Zn alloy in water

Neli Mintcheva [a, b], Ali A. Aljulaih [a, c], Shusuke Bito [a, c], Mitsuhiro Honda [a, d], Takahiro Kondo [a, e], Satoru Iwamori [c], Sergei A. Kulinich [a, *]

[a] Institute of Innovative Science and Technology, Tokai University, Hiratsuka, Kanagawa 259-1292, Japan
[b] Department of Chemistry, University of Mining and Geology, Sofia 1700, Bulgaria
[c] Department of Mechanical Engineering, Tokai University, Hiratsuka, Kanagawa 259-1292, Japan
[d] Graduate School of Engineering, Nagoya Institute of Technology, Nagoya, Aichi 466-8555, Japan
[e] Department of Chemistry, Gakushuin University, Toshima-ku, Tokyo 171-0031, Japan

ARTICLE INFO

Article history:
Received 23 December 2017
Received in revised form
14 February 2018
Accepted 28 February 2018
Available online 2 March 2018

Keywords:
Sn-Zn alloy
Laser ablation in liquid
Core@shell nanoparticles

ABSTRACT

Mixed oxides of Zn and Sn are of interest for gas sensing and diverse optoelectronic applications, and therefore new approaches to prepare such nanomaterials are anticipated. This study reports, for the first time, on the use of laser ablation in liquid applied to a Sn-Zn alloy and describes obtained products. Core@shell Sn@SnO and ZnO nanoparticles are shown to be produced by millisecond pulsed laser upon ablating eutectic Sn-Zn alloy in water. The as-prepared materials were found to contain surface hydroxide layers which were dehydrated to SnO_x and ZnO when higher laser energy fluence was applied or when the products were post-treated at 200C in air. The morphology, shape and size distribution, phase and chemical composition of prepared nanoparticles were studied as a function of laser parameters used during their preparation. Increase in pulse energy was found to result in fabrication of finer particles. It was found that while both metallic Sn and SnO_x were presented in the product, zinc was always oxidized to its oxide ZnO. In addition, when properly annealed, the produced nanomaterial demonstrated gas sensing response towards ammonia at room temperature.

1. Introduction

Laser ablation in liquid (LAL) is a versatile and easy-to-use technique for preparation of colloidal nanoparticles (NPs) of various chemical elements and their compounds, normally performed as a one-step and one-pot synthesis and permitting to minimize the amounts of used solvents and precursors [1–9]. Typically, a solid target (often metal) immersed in a liquid (water, ethanol, isopropanol, acetone, chloroform, etc.) is irradiated by pulsed laser beam to produce NPs whose composition, morphology, and other properties can be tuned by varying laser parameters and liquid medium [1–9]. Such laser parameters include: pulse wavelength and energy, pulse width, and repetition rate. In turn, such properties of the liquid medium as reactivity, thermal conductivity, temperature and pressure are also known to play a role in NP formation [1–9].

Apart from single-metal targets, ablation of alloys is a separate, and often much more challenging, task that aims at producing NPs with more complex and/or unique morphology and chemical composition. The latter purpose is proved to be even more difficult when NPs of two or more immiscible metals are targeted [10–12]. Though the idea of preparing alloy NPs through LAL is very attractive, as it could be a very simple and easy-to-perform approach, the number of studies in this area is quite limited, and no systematic work has been carried out, most of the reports being published as “case studies”. In some alloy systems, NPs with stoichiometry close to the target were obtained [13–17]. In some other systems, metal segregation was observed, thus giving rise to core@shell NPs in which the component with higher melting point makes the core, while the metal with lower melting point builds the shell layer. As an example, ablation of a composite Al-Ti target in isopropanol was reported to generate core@shell Ti@Al NPs [10].

Musaev et al. reported ablation of an eutectic BiInSn alloy in water and formation of three types of NPs with sizes 1 nm, 30 nm and 0.5 μm [18]. The mid-size ternary alloy NPs were observed in three phase states: amorphous uniform, crystalline uniform and crystalline segregated, the metal contents in all NPs differing from the initial ratio in the target [18]. The same effect was reported for

* Corresponding author.
E-mail address: skulinich@tokai-u.jp (S.A. Kulinich).

https://doi.org/10.1016/j.jallcom.2018.02.350
0925-8388/

other ablated alloys [16,17]. A number of studies was conducted on preparing quaternary chalcogenide or binary/ternary silicide NPs via pulsed LAL, and the technique was found to be an effective method to fabricate such nanomaterials via ablating alloy target or combined metal plates in different solvents and varying energy fluence and laser wavelengths [11,19–21].

Bimetallic NPs can be produced by various methods, including LAL [1–3]. In certain cases, the technique can be used to prepare NPs of alloys whose targets are unavailable or when constituent metals are immiscible in the bulk alloy. In doing so, one approach is laser irradiation of two colloids of individual NPs, where the composition of mixed-metal NPs can be tuned by the ratio of these metals in the initial colloidal mixture. As an example, laser irradiation by unfocused beam of Au and CoO NPs suspended in ethanol was reported to result in AuCo alloy NPs [22]. In another approach, a metal target is immersed into a colloid of a second metal [23,24] or into an aqueous solution of metal salt [25,26]. Intartaglia et al. reported on generation of bimetallic Ag-Au NPs by ablating Ag target in a suspension of Au NPs [27]. Interestingly, such alloy NPs were only achieved when wavelength of 355 and 532 nm was applied, while using the fundamental harmonic wavelength (1064 nm) led to a mixture of metallic Ag and Au NPs [27].

Zhang and coworkers produced NPs of Pt-Au alloy through ablation of hot-pressed mixture of platinum and gold powders as targets [12]. The composition of obtained NPs correlated well with the target Pt/Au ratio and was independent of set-up conditions such as media pH and applied laser fluence [12]. In a similar manner, Ni-Mo alloy NPs were attempted via LAL of pressed metal mixtures, demonstrating good results in acetone but not in water medium [28]. Amendola and co-workers provided a LAL-based synthetic route to Au-Fe and Ag-Fe alloy NPs whose components are immiscible and described how NP composition and structure depended on liquid media used [29].

NPs of tin and tin oxides have recently attracted much attention because of their catalytic, optoelectronic, conductive, redox properties which make them useful for applications in gas sensors, biosensors, lithium-storage materials, in rechargeable batteries or as photocatalysts that decay organic pollutants [30–37]. Although tin, as a low-melting-point metal, can be easily ablated, the number of works on LAL-prepared Sn-containing nanomaterials is quite limited, most authors mainly reporting various Sn and SnO_x NPs as product of metal tin ablation in ethanol and water, respectively [38,39].

Xiao et al. characterized their product LAL-generated in water as $Sn_6O_4(OH)_4$ nanocrystals, also observing their high photocatalytic performance [40]. LAL-generated SnO_x NPs were supported onto graphene oxide to form SnO_2/reduced-graphene-oxide nanocomposite which proved as excellent glucose sensor [41]. Non-stoichiometric tin oxide NPs prepared by nanosecond pulsed laser ablation of tin plate in water exhibited higher photodegradation effect on organic dyes, chlorophenol and Cr(VI) removal compared with their counterparts prepared by conventional methods [42]. Bao et al. reported Au@SnO_2 core@shell structures with a very high sensing response to H_2S at room temperature outperforming those of Au and SnO_2 NPs [43].

Mixed tin-zinc oxides were reported to be promising as nanomaterials with enhanced gas sensing or photocatalytic properties [44]. Although, based on the above, LAL is a very attractive and easy-to-use technique to prepare mixed-oxide nanomaterials, no Sn-Zn alloys were ablated so far. That is why, to study the potential of LAL in preparing mixed-oxide NPs of tin and zinc for gas sensing, in this work, eutectic Sn-Zn alloy (14.9 at.% of Zn) was ablated by millisecond pulsed laser in water medium. The choice of this alloy was dictated by its microstructural homogeneity, which was expected to provide uniform Zn/Sn ratio of ablated material across the target surface. The composition, morphology, size distribution and optical properties of the NPs produced under different conditions were then evaluated by structural, phase and optical methods. It was found that irrespective of laser parameters used, the products were hybrid nanomaterials based on ZnO and Sn@SnO core@shell NPs. After annealing in air, ammonia gas sensing was demonstrated at room temperature, implying that such nanomaterials may have promise as components of gas sensing devices.

2. Experimental section

The Sn-Zn alloy used in experiments (91% Sn and 9% Zn, or 14.9 at.% of Zn) was from the High Purity Chemicals Co., Japan. It was supplied as plates with 2 mm thickness and was used after cutting to proper pieces and degreasing in ethanol and water through sonication for 5 min.

LAL treatments of the target were carried out in a quartz cuvette ($30 \times 30 \times 50\ mm^3$ in size) filled with deionized water (15 mL). The exploited laser was millisecond pulsed Nd:YAG type with a wavelength of 1064 nm. The nanomaterials were produced at pulse peak power of 1 kW or 5 kW, and pulse width 0.5 ms or 2.0 ms, giving four experimental sets of laser conditions as follows: (A) peak power 1 kW and pulse width 0.5 ms; (B) peak power 1 kW and pulse width 2.0 ms; (C) peak power 5 kW and pulse width 0.5 ms; and (D) peak power 5 kW and pulse width 2.0 ms. Correspondingly, the produced samples are denoted as samples A-D, and the pulse energy was increased gradually from 0.5 to 10 J/pulse (see Table 1). In all experiments the repetition rate was kept at 3 Hz and the ablation time was 15 min. The alloy plate was placed vertically into a quartz cuvette and laser beam that irradiated the target through the cuvette side wall, was focused by a lens with the focal length of 9.0 cm. The beam diameter focused on the Sn/Zn target was ~150 μm. The setup and experimental procedures were similar to those previously described elsewhere [9,45,46]. The obtained materials were deposited as drops onto Cu grids for transmission electron microscopy (TEM, Hitachi HF-2200) studies. The suspensions were centrifuged at 16,500 rpm for 15 min, after which separated materials were drop-cast onto Si wafers for further characterization by X-ray photoelectron spectroscopy (XPS, Quantum 2000, ULVAC-PHI) and X-ray diffractometry (XRD, D8 Discover diffractometer from Bruker). UV–Vis absorption spectra of freshly prepared colloids were recorded by UV–Vis spectrophotometer (UV-2450, Shimadzu) in the wavelength range from 200 to 600 nm. Another set of samples prepared under same conditions was then annealed at 200C in air for 1 h and also analyzed.

Electron probe micro-analyzer (EPMA) was also employed to obtain information on chemical composition of the NPs. Distribution of O, Sn and Zn elements (elemental maping) was recorded over the surface of samples A and D (prepared with lowest- and highest-energy pulses) drop-cast onto Si wafers. The EPMA analysis was performed using a JEOL Superprobe JXA-8230 EPMA equipped with SEM and four wavelength-dispersive spectroscopy (WDS) spectrometers. The system provides SEM images and WDS elemental mapping of the same area. Gas sensing performance was evaluated at room temperature, in a standard chamber (5.4 L in volume) from Figaro. Ethanol, methanol, n-hexane, toluene, iso-

Table 1
Samples and laser conditions used for their preparation.

Sample	Pulse width (ms)	Pulse peak power (kW)	Pulse energy (J/pulse)
A	0.5	1	0.5
B	2.0	1	2.0
C	0.5	5	2.5
D	2.0	5	10

propanol and ammonia were used as target gases, while procedures were same as previously reported elsewhere [45,46].

3. Results and discussion

3.1. TEM results

The morphology and particle size of obtained materials were characterized by electron microscopy. The TEM images of the products prepared at peak power 1 kW and 5 kW are shown in Fig. 1a, b and c,d, respectively. It is seen in panels (a,b) that well-formed spherical NPs were obtained at lower pulse energies (samples A and B), their size being dependent on applied pulse width. At short pulse (0.5 ms), NPs with average diameters 30–60 nm are observed (Fig. 1a), while at longer pulse duration (2.0 ms), the particles decrease to 10–20 nm (Fig. 1b). This observation is most likely explained by the higher probability of secondary irradiation of already formed NPs by next photons and

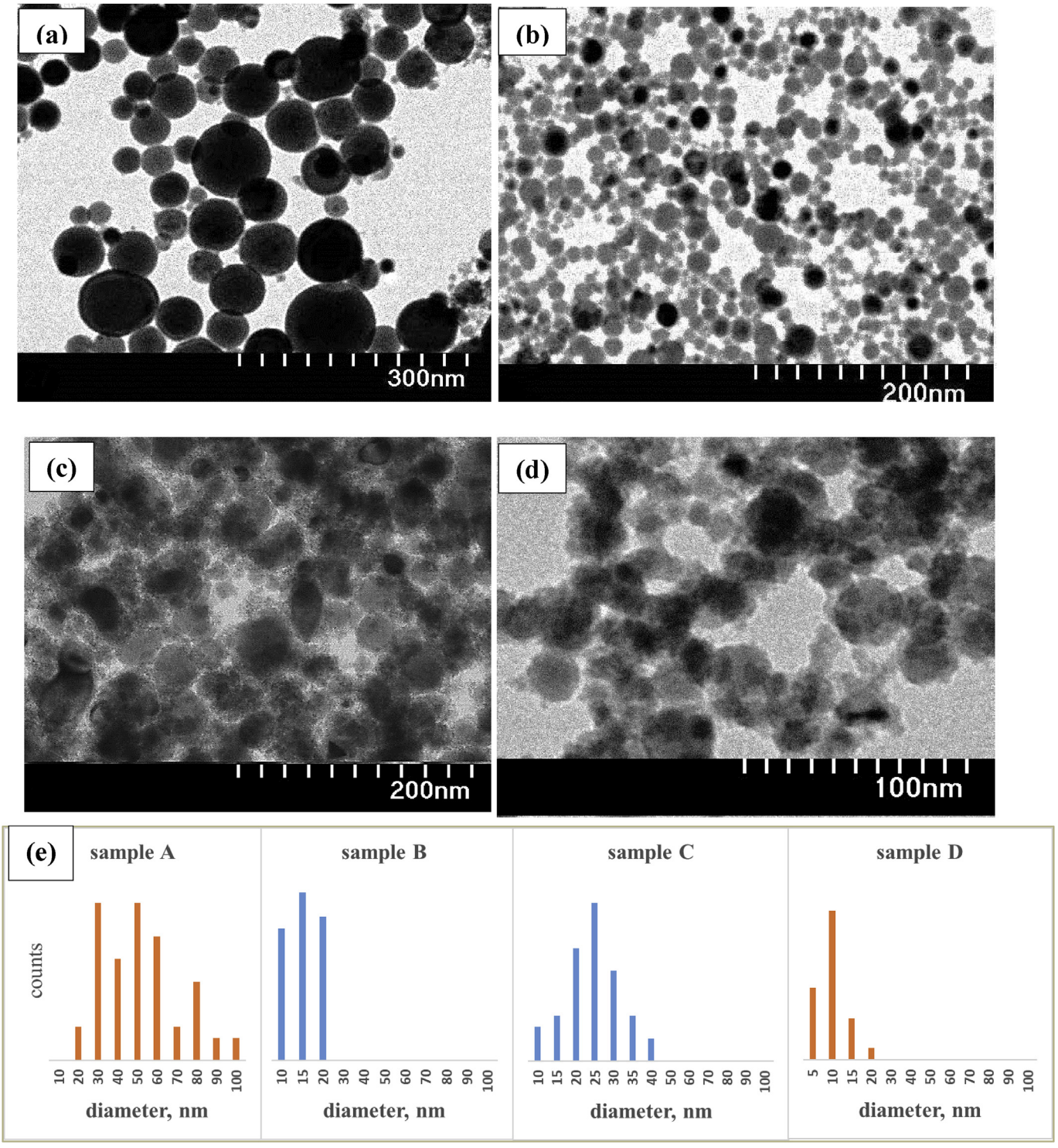

Fig. 1. TEM images of samples A, B, C and D in panels (a), (b), (c) and (d) respectively. Panel (e) shows size distribution of samples A – D.

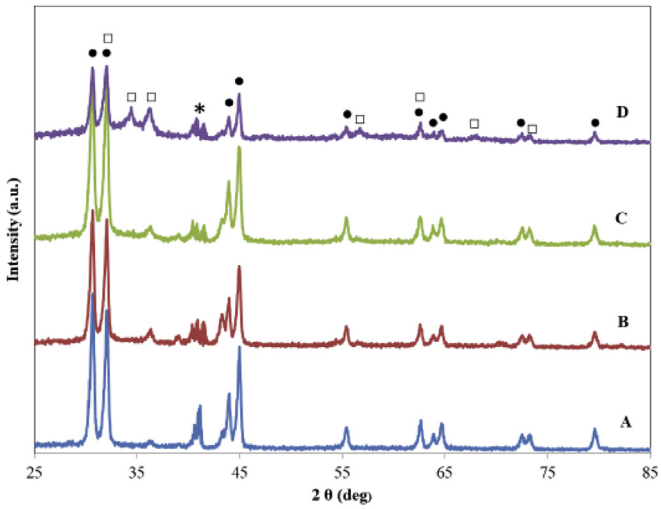

Fig. 2. XRD patterns of samples A, B, C and D. Sn and ZnO phases are denoted by solid circles (•) and empty squares (□), respectively. Multiple signal due to Si substrate is marked by asterisk.

pulses in case of longer pulses. Such an effect, often referred to as "secondary irradiation", was previously reported to be responsible for smaller sizes of LAL-generated NPs [1–3,5,9]).

The morphology of NPs changed to more irregular shapes in case of samples C and D, i.e. those prepared at higher pulse peak power of 5 kW (Fig. 1c and d). The average sizes in panels (c) and (d) are seen to be about 25 and 10 nm, respectively. This finding can also be explained by more intense secondary irradiation which is expected to fragment already formed NPs more efficiently at higher pulse power, thus giving rise to smaller and more irregular-shaped NPs. The histograms in Fig. 1e present particle size distribution for all the samples A-D. Sample A obtained with laser peak 1 kW and pulse width 0.5 ms is seen to demonstrate the broadest size distribution (Fig. 1a,e) where single spheres with diameter 90–100 nm, as well as smaller ones down to 20 nm can be seen, while sample B shows the narrowest size range resulted from NP fragmentation.

Note that, similar to the previously reported results on LAL-prepared SnO_x nanomaterials also produced with ms-long pulses [45], many NPs in Fig. 1 appear to be core@shell structures, presumably having $Sn@SnO_x$ structure. At the same time, unlike the report of Honda and co-workers on ZnO nanorods produced with ms-pulsed laser via ablation of zinc target in water [9], no nanorods are observed in Fig. 1. This is probably explained by the fact that small ZnO nuclei (the presence of ZnO being confirmed by other techniques below) could not agglomerate and recrystallize as larger nanorods since the product's bulk was dominated by Sn-based materials.

3.2. X-ray diffraction patterns and EPMA results

XRD patterns of produced NPs are shown on Fig. 2. Diffraction peaks corresponding to metallic Sn (JCPDS card no. 00-004-0673) are observed for all samples. As clearly seen in Fig. 2 (purple pattern), which shows XRD pattern of sample D, the diffraction peaks indicate a mixture of Sn and ZnO. The peaks of ZnO are well consistent with the hexagonal ZnO phase (JCPDS card no. 00-024-1342) [6,8,9]. Interestingly, all previous works on LAL of metallic Sn in water reported various SnO_x [30,38,40–42], while in this study, according to XRD, the products of Sn-Zn alloy ablation demonstrate metallic Sn as the main phase. At the same time, the patterns in Fig. 2 agree well with the recent results reported by Honda *et al* [45]. It was found that the NPs produced via LAL of pure Sn in water by means of ms-laser were $Sn@SnO_x$ structures, while the use of pulses with the highest energy of 10 J/pulse produced mainly $SnO@SnO_x$ NPs (note that XRD patterns reported in Ref. [45] were very similar to those in Fig. 2). The XRD pattern of sample D (purple line), prepared at the highest pulse energy of 10 J/pulse, also implies that SnO phase could form in the sample, which cannot be concluded clearly as the XRD peaks of SnO overlap with those of ZnO (empty squares in Fig. 2).

Figs. 3 and 4 present WDS elemental mapping of products prepared with the lowest and highest pulse energies (0.5 and 10 J/pulse, see Table 1), respectively. Both figures exhibit SEM images in panel (a) and WDS elemental mapping images of the same area which show the distribution of oxygen (b), tin (c) and zinc (d) across the same area. The following conclusions can be drawn from the WDS mapping images in Figs. 3 and 4. (1) Smaller Sn-rich and Zn-rich NPs are clearly observed in Fig. 4 when compared with Fig. 3, which agrees well with the TEM images in Fig. 1. (2) The areas rich in Zn are typically associated with those rich in oxygen but depleted of tin, thus implying the presence of ZnO (marked with white oval frames in Figs. 3 and 4). (3) The areas rich in Sn are often depleted of both oxygen and zinc, which lends support to the existence of metallic Sn NPs and their agglomerates (marked with rectangular frames in Figs. 3 and 4). (4) Some large areas have all the three elements available (see yellow square frames in Figs. 3 and 4), demonstrating more homogeneous mixtures of several phases. (5) Unlike the initial alloy target, the elements in the product are not distributed homogeneously, and phases appear to be separated so that there are ZnO and $Sn@SnO_x$ NPs of different sizes. The latter metallic-tin containing NPs constitute a large part of the product, which makes the as-prepared material apparently conductive and not suitable for gas sensing.

3.3. UV–vis spectroscopy

UV–Vis absorption spectra of as-prepared suspensions A – D are shown in Fig. 5. For samples A – C, the absorption band observed at 250–260 nm can be assigned to the plasmon resonance of metallic Sn NPs. Recently, NPs LAL-generated with ns- and ms-long pulses were reported to demonstrate peaks of metallic Sn at ~290 and ~280 nm, respectively [45]. A wide band centred at 250 nm for sample A (blue spectrum) is due to the absorption of NPs with various sizes, which is consistent with the sizes observed by TEM (Fig. 1a).

Blue shift is observed for all samples in comparison with the bulk metal (Sn) and it correlates with the decrease in NP size in the row: A > C > B > D. The same trend can be seen in the size distribution histograms presented in Fig. 1e. In the spectrum of sample D (Fig. 5, purple line), the peak caused by metallic Sn NPs shifts towards 200 nm and corresponds to a significant decrease of the NP size (<10 nm), which is also supported by the TEM image in Fig. 1d.

The absorption spectra of samples C and D (green and purple lines) show weak shoulders around 400 and 350 nm derived from tin oxides. Previously, a similar absorption band at ~400 nm was reported for SnO_x obtained via LAL of pure Sn in water using millisecond pulsed laser [45]. The band at 350 nm in spectrum D may also have some contribution from UV absorption of ZnO NPs [9] as sample D was shown in Fig. 2 to have more ZnO.

3.4. X-ray photoelectron spectroscopy

XPS spectra provide substantial information about the surface chemical composition and oxidation states of the elements, analyzing surface layers of NPs as thick as several nm. The O 1s, Sn $3d_{5/2}$ and Zn $2p_{3/2}$ XPS spectra of samples A - D, both as-prepared

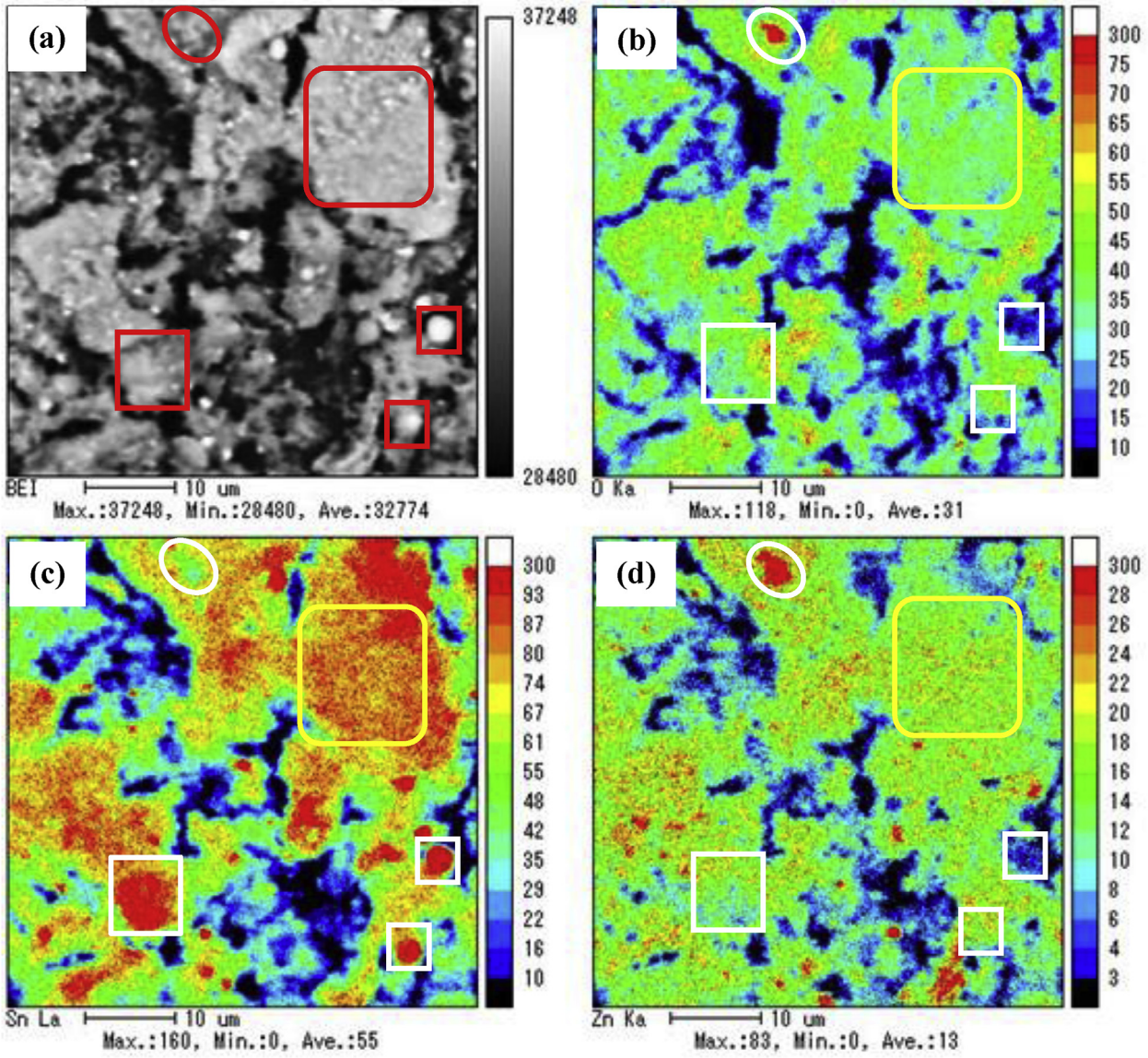

Fig. 3. EPMA analysis of sample A drop-cast onto Si wafer. (a) SEM image, (b)–(d) corresponding WDS mapping images for oxygen (b), tin (c) and zinc (d). White oval and rectangular frames indicate areas rich in Zn and Sn, respectively, while yellow square frames show those where all the three elements are detected. All these areas are discussed in greater detail in the text. (For interpretation of the references to colour in this figure legend, the reader is referred to the Web version of this article.)

and annealed, are presented in Figs. 6–8, respectively. In all the figures, panel (a) presents spectra of the as-prepared samples A - D drop-cast onto Si wafers and dried, while panel (b) presents those of the same samples heat-treated in air for 1 h at 200C.

Both as-prepared samples A and B are seen in Fig. 6a (blue and red lines) to have the signal of hydroxyl group as the main oxygen species on their surface (indicated by red vertical line) [9,45,47]. The O 1s spectra of samples C and D prepared with higher-energy pulses are seen in Fig. 6a to become asymmetric, demonstrating that two additional species, ZnO and SnO_x emerged in the samples [9,45,47]. Thus, when pulses with higher energy are applied, this leads to gradual surface dehydration of the produced NPs, which could be associated with higher temperatures generated around ablated zone by such pulses. This agrees well with the narrow scan spectra of Sn and Zn discussed in more detail below.

The Sn $3d_{5/2}$ peaks of as-prepared samples A, B and C in Fig. 7a are seen to have metallic Sn, Sn(II) and Sn(IV) species on their surface (vertical lines in Fig. 7a), while the metallic Sn(0) component disappears in sample D (purple spectrum in Fig. 7a) [38,42,50–55]. This agrees well with the oxygen XPS spectra in Fig. 6a, confirming more advanced surface oxidation of produced NPs when pulses with larger pulse energy are applied [38,42]. Somewhat similarly, the XPS Zn $2p_{3/2}$ peaks of as-prepared samples A and B demonstrate Zn-OH bonds as the dominating surface species (red vertical line in Fig. 8a) [9,48], while the contribution of the ZnO binding gradually increases in samples C and D (blue vertical line) [49–51]. This implies that NP surface gets gradually dehydrated when laser pulses with higher energy ablate the target. The formation of ZnO is also confirmed by the absorption band detected at 350 nm in the UV–vis spectrum of sample D (Fig. 5, purple spectrum). Thus, the surface of the as-prepared samples A – B is mainly formed by metal hydroxides which tend to be partially dehydrated and turn to oxides, ZnO and SnO_x, in samples C and D prepared at higher laser fluence.

During annealing at 200C for 1 h, surface metal hydroxides $Sn(OH)_x$ and $Zn(OH)_2$ were found to undergo transformation to

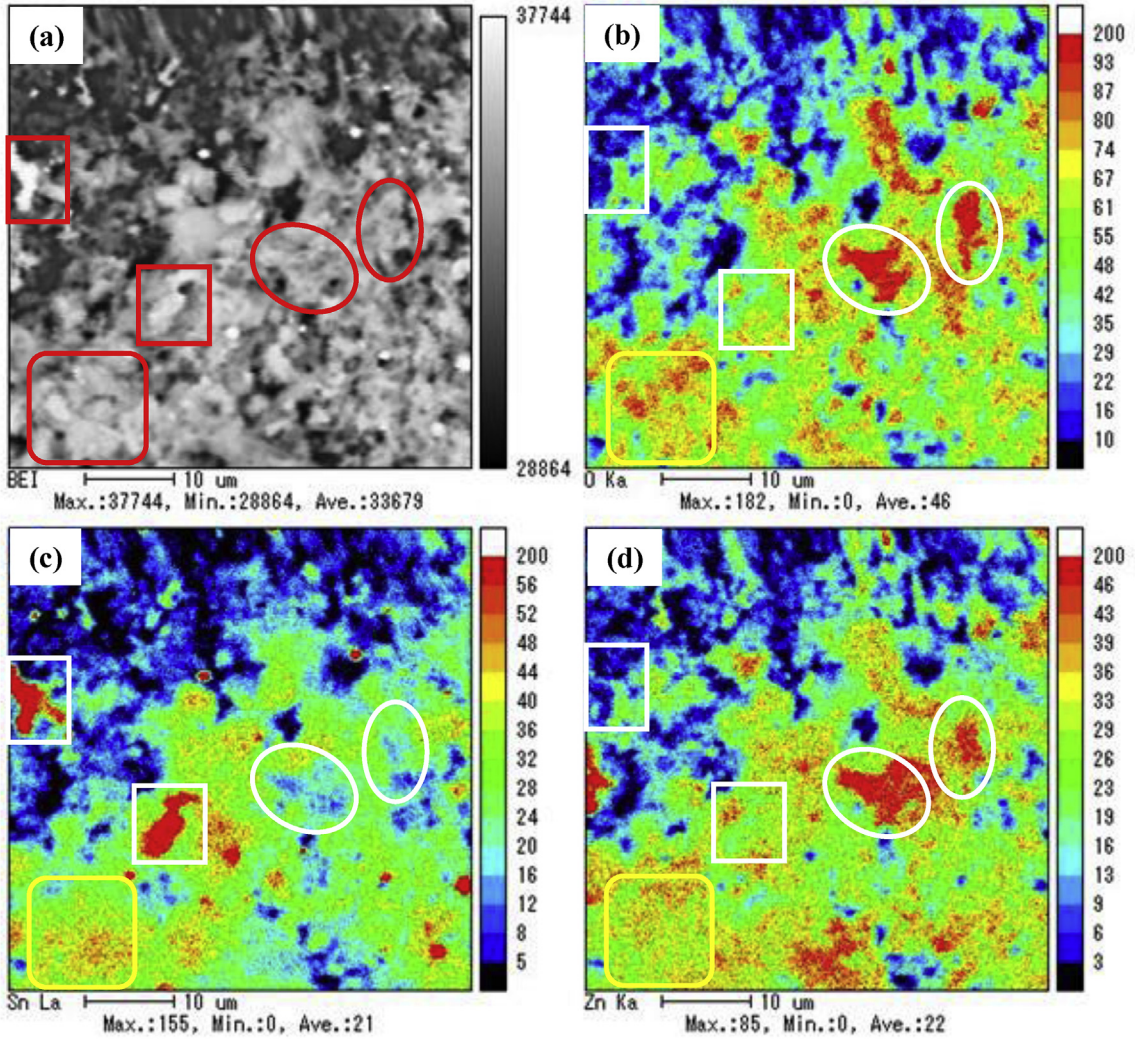

Fig. 4. EPMA analysis of sample D drop-cast on Si wafer. (a) SEM image; (b)–(d) corresponding WDS mapping images for oxygen (b), tin (c) and zinc (d). White oval and rectangular frames indicate areas rich in Zn and Sn, respectively, while yellow square frames show those where all the three elements are detected. All these areas are discussed in greater detail in the text. (For interpretation of the references to colour in this figure legend, the reader is referred to the Web version of this article.)

their corresponding oxides. This is well seen as increased intensities of spectra around binding energies for ZnO and SnO_x, respectively (Fig. 6b). The same is observed in Fig. 8b, where all Zn

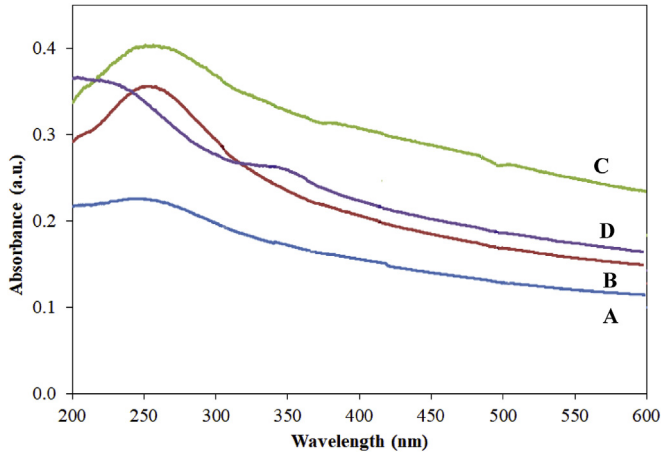

Fig. 5. UV–Vis spectra of as-prepared suspensions of samples A, B, C and D.

peaks are significantly shifted from the binding energy of $Zn(OH)_2$ to ZnO (Fig. 8a and b). The latter shift of the XPS Zn 2p peaks of the annealed samples from $Zn(OH)_2$ to ZnO implies the dominance of the hydroxyl groups on ZnO surface in the as-prepared NPs and confirms that gradual surface dehydration occurs at elevated temperatures both during preparation or annealing. Thus, $Zn(OH)_2$ dominates in as-prepared samples A, B and C (Fig. 8a), while on the surface of annealed materials and that of as-prepared sample D the contribution of ZnO species becomes significant (Fig. 8a and b). This is in agreement with XRD data (Fig. 2, purple pattern) and UV–vis spectrum of sample D (Fig. 5, purple line).

Annealing of nanomaterials at 200C does not cause significant changes in the oxidation state of Sn, which mainly remains as Sn(II) (red vertical line in Fig. 7), however metallic signal (blue vertical line in Fig. 7b) disappears, implying gradual oxidation during heat treatment in air. Interestingly, the fraction of Sn(IV) in all annealed samples is seen in Fig. 7b to be only slightly increased (green vertical line) [38,54–56]. This is believed to be explained by a relatively slow diffusion of oxygen through the SnO_x shell that covered the NPs. Meanwhile, the oxidation of the shells themselves and formation of SnO_2 phase from SnO was very limited at such a low annealing temperature (200C).

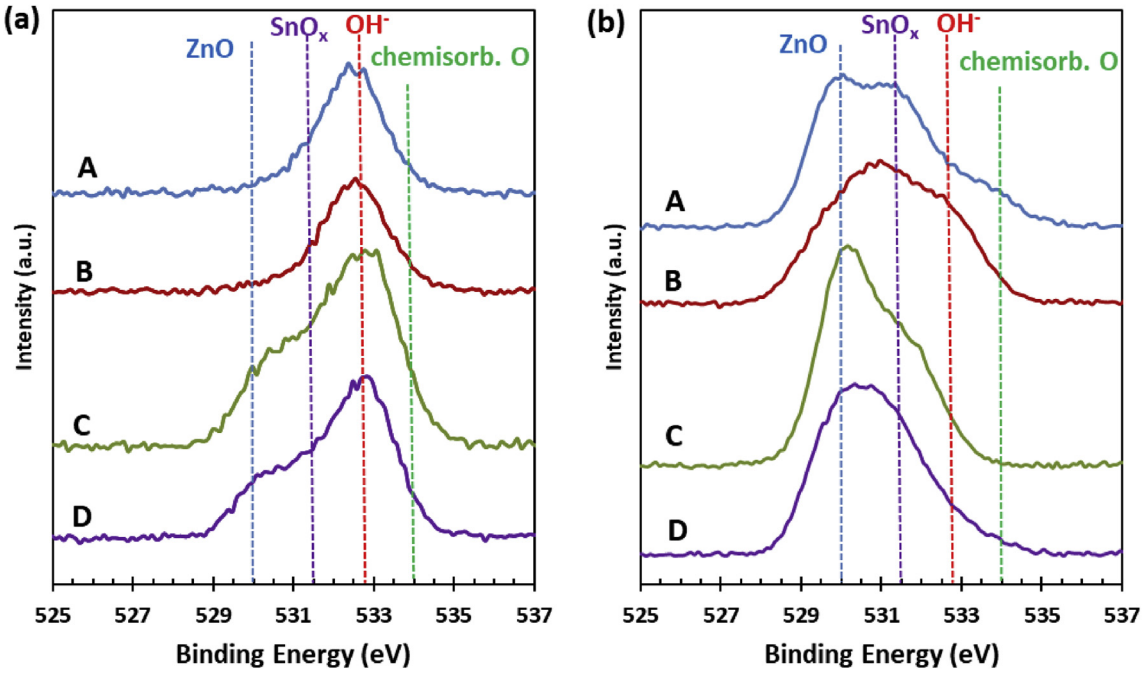

Fig. 6. XPS O 1s spectra of samples A, B, C and D: (a) as-prepared and drop-cast and (b) annealed at 200C for 1 h. Vertical dashed lines demonstrate position of oxygen bonding in ZnO, SnO_x, OH^-, and chemisorbed oxygen.

Thus, the XPS measurements confirmed the above mentioned findings that hybrid nanomaterials of ZnO, SnO_x and Sn@SnO_x NPs, as main components, were prepared. While the surface of as-prepared NPs was considerably hydrated, annealing at 200C in air led to gradual dehydration and transition from hydroxides to oxides. In parallel, the SnO_x phase was gradually oxidized during annealing, turning slowly from SnO to SnO_2. These two major transformations caused by heat treatment were further used to prepare a gas sensor based on the as-prepared sample D.

3.5. Gas sensing towards NH_3

The use of both ZnO and SnO_x nanomaterials in gas sensing devices is well known, as these two materials are the most studied components of chemiresistive gas sensors [45,46]. Composites of ZnO and SnO_x, or their doped/hybrid oxides, were reported to perform even better than their single-component oxides [57–60]. For instance, in works [57–60] good sensing of various ZnO-SnO_x composites towards ethanol, humidity, hydrogen and ozone was

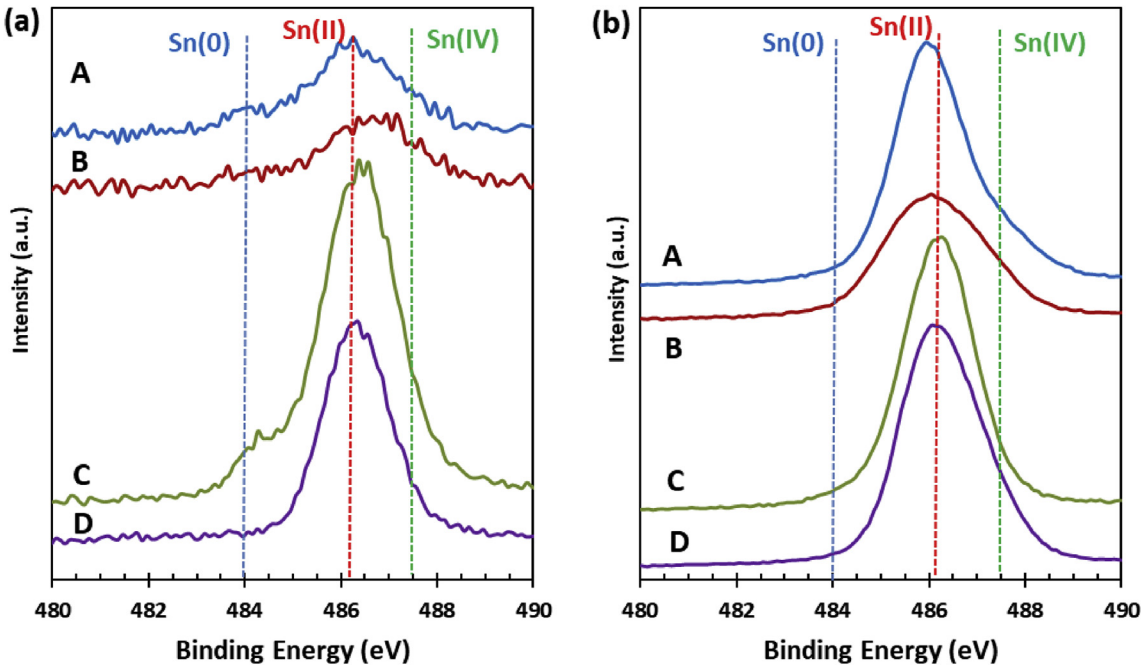

Fig. 7. XPS Sn $3d_{5/2}$ spectra of samples A, B, C and D: (a) as-prepared and drop-cast and (b) annealed at 200C for 1 h. Vertical dashed lines demonstrate position of Sn bonding in metallic Sn(0), Sn(II), and Sn(IV).

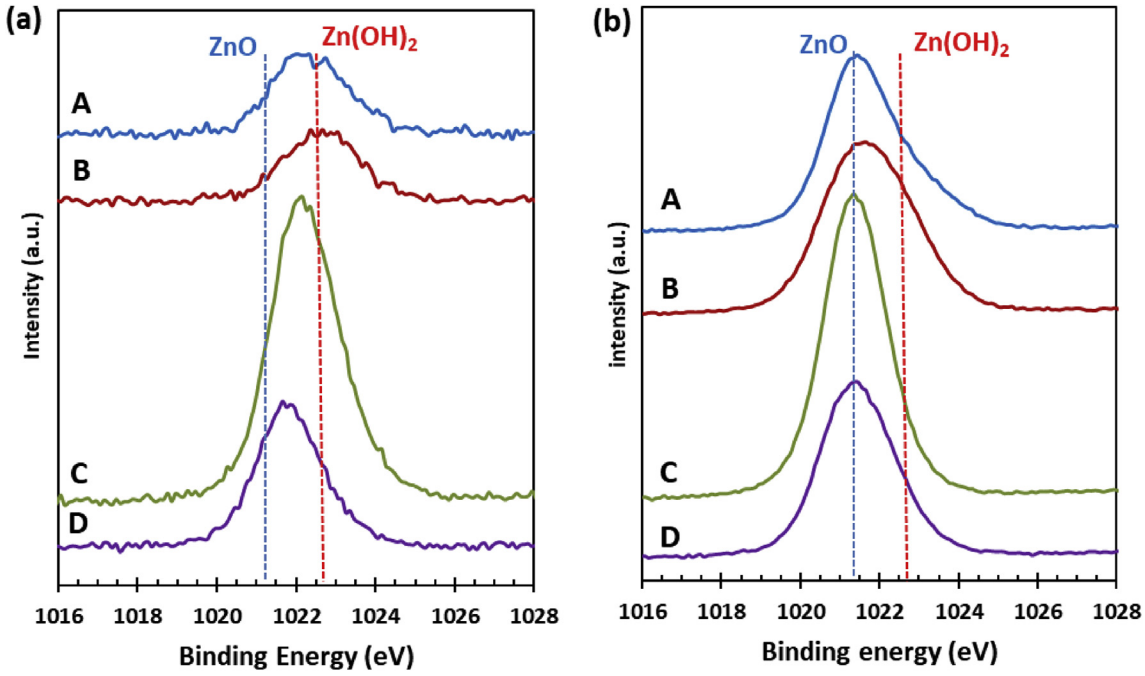

Fig. 8. XPS Zn $2p_{3/2}$ spectra of samples A, B, C and D: (a) as-prepared and drop-cast and (b) annealed at 200C for 1 h. Vertical dashed lines demonstrate position of Zn bonding in ZnO and $Zn(OH)_2$.

reported. At the same time, gas sensing devices working at room temperature are still rare and highly anticipated [45,46,60]. Since in our previous studies, room temperature sensing of LAL-prepared NPs of SnO_x [45] and ZnO [46] was reported, the present work was stimulated by potential gas sensing properties of the prepared nanomaterials as hybrid oxide NPs of zinc and tin were expected.

As was mentioned in section 3.2, the as-prepared materials were rich in metallic Sn, and thus they had to be heat-treated to oxidize such NPs, making them semiconducting and proper for gas-sensing application. Accordingly, sample D was drop-cast on an interdigitated electrode and annealed for 9 h in air at 200C, after which it was tested in presence of several gases (as potential target gases). Of all the gases (ethanol, methanol, iso-propanol, n-hexane, toluene and ammonia), the sample only responded to ammonia, thus demonstrating good selectivity. Fig. 9 presents the response curve towards 250 ppm of ammonia at room temperature. The gas response S (%) calculated as $(R_a\text{-}R_g)x100/R_a$ was ~92%, implying that lower concentrations can also be detected. The response time was ~4 min, which is comparable with 3 min recently reported by Ghule and coauthors for carbon-based sensor working at 80C and detecting as little as 100 ppm of ammonia with S = 50% [61].

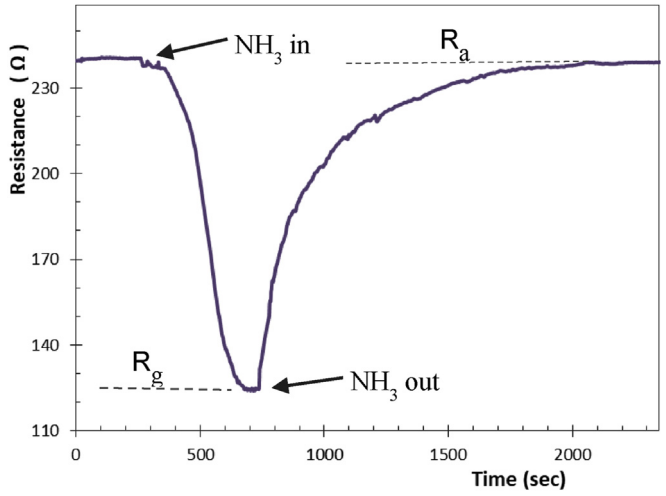

Fig. 9. Response curve at room temperature of sample D annealed for 9 h in air at 200C towards ammonia (250 ppm). Response time was found to be ~4 min. Gas response S (%) calculated as $(R_a\text{-}R_g)$ x $100/R_a$ was ~92%.

Note that the results presented in Fig. 9 are preliminary, as the sensor prepared via annealing was not optimized. Its parameters, such as NP layer thickness, annealing time, duration and temperature, are still to be studied and improved. More detailed optimization and development of gas-sensing devices based on all samples A-D is a subject of further studies. Nevertheless, the preliminary results obtained in this report show that nanomaterials produced via laser ablation of Sn-Zn alloys can be regarded as promising candidates for low-operating-temperature NH_3 sensors.

4. Conclusions

New tin- and zinc-containing nanomaterials were prepared by laser ablation in liquid method applied to eutectic Sn-Zn alloy (91% Sn and 9% Zn). Irradiation of the alloy with millisecond pulsed laser causes segregation of metals and formation of ZnO nanoparticles and $Sn@SnO_x$ core@shell nanoparticles. The size, morphology and composition of nanoparticles are effected by laser parameters and post-synthesis treatment. At higher and lower laser pulse power, nanoparticles with sizes 10–20 and 10–100 nm, respectively, were observed. According to XPS, the surface of as-prepared products was mainly metal hydroxides, $Sn(OH)_2$ and $Zn(OH)_2$. After annealing, the materials demonstrated gradual surface dehydration and further oxidation. Preliminary gas-sensing tests showed that after proper heat-treatment, the produced nanomaterials demonstrated highly-selective response towards ammonia, implying that such nanomaterials produced via laser ablation are good candidates for gas sensing devices operating at low temperatures.

Acknowledgements

The authors are grateful to the Japan Society for the Promotion of Science (JSPS) for support of this research (grant nos. 16K04904 and 15K17431). S.A.K. and M.H. thank the support from the Daiwa Anglo-Japanese Foundation (Daiwa Foundation Award 11425/12174). Finally, N.M. thanks Tokai University for exchange research grant.

References

[1] D.S. Zhang, J. Liu, C.H. Liang, Perspective of how laser-ablated particles grow in liquids, Sci. China Phys. Mech. Astron. 60 (2017), 074201.
[2] J. Xiao, P. Liu, C.X. Wang, G.W. Yang, External field-assisted laser ablation in liquid: an efficient strategy for nanocrystal synthesis and nanostructure assembly, Prog. Mater. Sci. 87 (2017) 140–220.
[3] H.B. Zeng, X.W. Du, S.C. Singh, S.A. Kulinich, S.K. Yang, J.P. He, W.P. Cai, Nanomaterials via laser ablation/irradiation in liquid: a review, Adv. Funct. Mater. 22 (2012) 1333–1353.
[4] K.Y. Niu, J. Yang, S.A. Kulinich, J. Sun, X.W. Du, Hollow nanoparticles of metal oxides and sulfides: fast preparation via laser ablation in liquid, Langmuir 26 (2010) 16652–16657.
[5] K.Y. Niu, J. Yang, S.A. Kulinich, J. Sun, H. Li, X.W. Du, Morphology control of nanostructures via surface reaction of metal nanodroplets, J. Am. Chem. Soc. 132 (2010) 9814–9819.
[6] S.A. Kulinich, T. Kondo, Y. Shimizu, T. Ito, Pressure effect on ZnO nanoparticles prepared via laser ablation in water, J. Appl. Phys. 113 (2013), 033509.
[7] M. Koizumi, S.A. Kulinich, Y. Shimizu, T. Ito, Slow dynamics of ablated zone observed around the density fluctuation ridge of fluid medium, J. Appl. Phys. 114 (2013), 214301.
[8] T. Goto, M. Honda, S.A. Kulinich, Y. Shimizu, T. Ito, Defects in ZnO nanoparticles laser-ablated in water-ethanol mixture at different pressures, Jpn. J. Appl. Phys. 54 (2015), 070305.
[9] M. Honda, T. Goto, T. Owashi, A.G. Rozhin, S. Yamaguchi, T. Ito, S.A. Kulinich, ZnO nanorods prepared via ablation of Zn with millisecond laser in liquid media, Phys. Chem. Chem. Phys. 18 (2016) 23628–23637.
[10] A.A. Serkov, E.V. Barmina, A.V. Simakin, P.G. Kuzmin, V.V. Voronov, Generation of core-shell nanoparticles Al@Ti by laser ablation in liquid for hydrogen storage, Appl. Surf. Sci. 348 (2015) 71–74.
[11] M.I. Mendivil, L.V. Garcia, B. Krishnan, D. Avellaneda, J.A. Martinez, S. Shaji, $CuInGaSe_2$ nanoparticles by pulsed laser ablation in liquid medium, Mater. Res. Bull. 72 (2015) 106–115.
[12] J. Zhang, D.N. Oko, S. Garbarino, R. Imbeault, M. Chaker, A.C. Tavares, D. Guay, D. Ma, Preparation of PtAu alloy colloids by laser ablation in solution and their characterization, J. Phys. Chem. C 116 (2012) 13413–13420.
[13] O. Olea-Mejía, M. Fernández-Mondragón, G. Rodríguez-de la Concha, M. Camacho-López, SERS-active Ag, Au and Ag–Au alloy nanoparticles obtained by laser ablation in liquids for sensing methylene blue, Appl. Surf. Sci. 348 (2015) 66–70.
[14] I.A. Sukhov, G.A. Shafeev, V.V. Voronov, M. Sygletou, E. Stratakis, C. Fotakis, Generation of nanoparticles of bronze and brass by laser ablation in liquid, Appl. Surf. Sci. 302 (2014) 79–82.
[15] J. Jakobi, A. Menéndez-Manjón, V.S.K. Chakravadhanula, L. Kienle, P. Wagener, S. Barcikowski, Stoichiometry of alloy nanoparticles from laser ablation of PtIr in acetone and their electrophoretic deposition on PtIr electrodes, Nanotechnology 22 (2011), 145601.
[16] J. Jakobi, S. Petersen, A. Menéndez-Manjón, P. Wagener, S. Barcikowski, Magnetic alloy nanoparticles from laser ablation in cyclopentanone and their embedding into a photoresist, Langmuir 26 (2010) 6892–6897.
[17] I. Lee, S.W. Han, K. Kim, Production of Au–Ag alloy nanoparticles by laser ablation of bulk alloys, Chem. Commun. (2001) 1782–1783.
[18] O.R. Musaev, E. Sutter, J.M. Wrobel, M.B. Kruger, Structures of BiInSn nanoparticles formed through laser ablation, Appl. Phys. A 110 (2013) 329–333.
[19] N. Tarasenka, V. Pankov, A. Butsen, N. Tarasenko, Laser assisted synthesis, structural and magnetic characterization of gadolinium germano-silicide nanoparticles in liquid, J. Nanosci. Nanotechnol. 16 (2016) 7451–7460.
[20] N. Tarasenka, A. Butsen, V. Pankov, N. Tarasenko, Structural defects and magnetic properties of gadolinium silicide nanoparticles synthesized by laser ablation technique in liquid, Phys. Status Solidi B 250 (2013) 809–814.
[21] N.V. Tarasenko, A.V. Butsen, M.I. Nedelko, N.N. Tarasenka, Laser-aided preparation and modification of gadolinium silicide nanoparticles in liquid, J. Phys. Chem. C 116 (2012) 3897–3902.
[22] Z. Swiatkowska-Warkocka, K. Koga, K. Kawaguchi, H. Wang, A. Pyatenko, N. Koshizaki, Pulsed laser irradiation of colloidal nanoparticles: a new synthesis route for the production of non-equilibrium bimetallic alloy submicrometer spheres, RSC Adv. 3 (2013) 79–83.
[23] M. Vinod, K.G. Gopchandran, Bimetallic Au-Ag nanochains as SERS substrates, Curr. Appl. Phys. 15 (2015) 857–863.
[24] S. Petrović, D. Milovanović, B. Salatić, D. Peruško, J. Kovač, G. Dražić, M. Mitrić, M. Trtica, B. Jelenković, Composition and structure of NiAu nanoparticles formed by laser ablation of Ni target in Au colloidal solution, Mater. Chem. Phys. 166 (2015) 223–232.
[25] P. Liu, H. Chen, H. Wang, J. Yan, Z. Lin, G. Yang, Fabrication of Si/Au core/shell Nanoplasmonic structures with ultrasensitive surface-enhanced Raman scattering for monolayer molecule detection, J. Phys. Chem. C 119 (2015) 1234–1246.
[26] Z. Sheykhifard, M. Ranjbar, H. Farrokhpour, H. Salamati, Direct fabrication of Au/Pd(II) colloidal core-shell nanoparticles by pulsed laser ablation of gold in $PdCl_2$ solution, J. Phys. Chem. C 119 (2015) 9534–9542.
[27] R. Intartaglia, G. Das, K. Bagga, A. Gopalakrishnan, A. Genovese, M. Povia, E. Di Fabrizio, R. Cingolani, A. Diaspro, F. Brandi, Laser synthesis of ligand-free bimetallic nanoparticles for plasmonic application, Phys. Chem. Chem. Phys. 15 (2013) 3075.
[28] G. Marzun, A. Levish, V. Mackert, T. Kallio, S. Barcikowski, P. Wagener, Laser synthesis, structure and chemical properties of colloidal nickel-molybdenum nanoparticles for the substitution of noble metals in heterogeneous catalysis, J. Colloid Interface Sci. 489 (2017) 57–67.
[29] S. Scaramuzza, S. Agnoli, V. Amendola, Metastable alloy nanoparticles, metal-oxide nanocrescents and nanoshells generated by laser ablation in liquid solution: influence of the chemical environment on structure and composition, Phys. Chem. Chem. Phys. 17 (2015) 28076–28087.
[30] L.L. Wang, L.P. Kang, H.Y. Wang, Zh P. Chen, X.J. Li, Capacitive humidity sensitivity of SnO_2:Sn thin film grown on silicon nanoporous pillar array, Sens. Actuators, B 229 (2016) 513–519.
[31] G. Lu, L. Ocola, J. Chen, Room-temperature gas sensing based on electron transfer between discrete tin oxide nanocrystals and multiwalled carbon nanotubes, Adv. Mater. 21 (2009) 2487–2491.
[32] L.L. Wang, Z.J. Li, L. Luo, C.Z. Zhao, L.P. Kang, D.W. Liu, Methanol sensing properties of honey-like SnO_2 grown on silicon nanoporous array, J. Alloys Compd. 682 (2016) 170–175.
[33] L.F. Zhu, M.G. Wang, T.K. Lam, C.G. Zhang, H.D. Du, B.H. Li, Y.W. Yao, Fast microwave-assisted synthesis of gas-sensing SnO_2 quantum dots with high sensitivity, Sens. Actuators B 236 (2016) 646–653.
[34] S.H. Li, Z. Chu, F.F. Meng, T. Luo, X.Y. Hu, S.Z. Huang, Z. Jin, Highly sensitive gas sensor based on SnO_2 nanorings for detection of isopropanol, J. Alloys Compd. 688 (2016) 712–717.
[35] A. Kolmakov, Y. Zhang, G. Cheng, M. Moskovits, Detection of CO and O_2 using tin oxide nanowire sensors, Adv. Mater. 15 (2003) 997–1000.
[36] Y. Idota, T. Kubota, A. Matsufuji, Y. Maekawa, T. Miyasaka, Tin-based amorphous oxide: a high-capacity lithium-ion-storage material, Science 276 (1997) 1395–1397.
[37] Z.Y. Yu, R.Y. Qiu, H.R. Li, Z.Y. Wang, X.H. Ma, C.N. Dong, Preparation and photocatalytic activity of SnO_2, Mater. Lett. 170 (2016) 25–30.
[38] O.R. Musaev, M.S. Driver, E.A. Sutter, A.N. Caruso, J.M. Wrobel, M.B. Kruger, Influence of the liquid environment on the products formed from the laser ablation of tin, Appl. Phys. A 113 (2013) 355–359.
[39] M.K. Singh, M.C. Mathpal, A. Agarwal, Optical properties of SnO_2 quantum dots synthesized by laser ablation in liquid, Chem. Phys. Lett. 536 (2012) 87–91.
[40] J. Xiao, Q.L. Wu, P. Liu, Y. Liang, H.B. Li, M.M. Wu, G.W. Yang, Highly stable sub-5 nm $Sn_6O_4(OH)_4$ nanocrystals with ultrahigh activity as advanced photocatalytic materials for photodegradation of methyl orange, Nanotechnology 25 (2014), 135702.
[41] Y. Ye, P. Wang, E. Dai, J. Liu, Z. Tian, C. Liang, G. Shao, A novel reduction approach to fabricate quantum-sized SnO_2-conjugated reduced graphene oxide nanocomposites as non-enzymatic glucose sensors, Phys. Chem. Chem. Phys. 16 (2014) 8801–8807.
[42] Z. Tian, C. Liang, J. Liu, H. Zhang, L. Zhang, Reactive and photocatalytic degradation of various water contaminants by laser ablation-derived SnO_x nanoparticles in liquid, J. Mater. Chem. 21 (2011) 18242–18247.
[43] H. Bao, Y. Wang, H. Zhang, Q. Zhao, G. Liu, W. Cai, Ultrathin tin oxide layer-wrapped gold nanoparticles induced by laser ablation in solutions and their enhanced performances, J. Colloid Interface Sci. 489 (2017) 92–99.
[44] A. Katoch, J.H. Kim, Y.J. Kwon, H.W. Kim, S.S. Kim, Bifunctional sensing mechanism of SnO_2-ZnO composite nanofibers for drastically enhancing the sensing behavior in H_2 gas, ACS Appl. Mater. Interfaces 7 (2015) 11351–11358.
[45] M. Honda, T. Kondo, T. Owashi, P. Shankar, S. Iwamori, Y. Ichikawa, S.A. Kulinich, Nanostructures prepared via laser ablation of tin in water, New J. Chem. 41 (2017) 11308–11316.
[46] T. Kondo, Y. Sato, M. Kinoshita, P. Shankar, N.N. Mintcheva, M. Honda, S. Iwamori, S.A. Kulinich, Room temperature ethanol sensor based on ZnO prepared via laser ablation in water, Jpn. J. Appl. Phys. 56 (2017), 080304.
[47] Handbook of X-ray Photoelectron Spectroscopy, Physical Electronics, Perkin-Elmer Corporation, Minnesota, USA, 1992, p. 44, 88, 126.
[48] B.C. Lin, P. Shen, S.Y. Chen, ZnO and ε-$Zn(OH)_2$ composite nanoparticles by pulsed laser ablation on Zn in water, J. Phys. Chem. C 115 (2011) 5003–5010.
[49] R. Al-Gaashani, S. Radiman, A.R. Daud, N. Tabet, Y. Al-Douri, XPS and optical studies of different morphologies of ZnO nanostructures prepared by microwave methods, Ceram. Int. 39 (2013) 2283–2292.
[50] J. Liu, T. Wang, B. Wang, P. Sun, Q. Yang, X. Liang, H. Song, G. Lu, Highly sensitive and low detection limit of ethanol gas sensor based on hollow ZnO/SnO_2 spheres composite material, Sens. Actuators B 245 (2017) 551–559.
[51] X. Li, X. Cao, L. Xu, L. Liu, Y. Wang, C. Meng, Z. Wang, High dielectric constant in Al-doped ZnO ceramics using high pressure treated powders, J. Alloys Compd. 657 (2016) 90–94.

[52] M. Kwoka, L. Ottaviano, M. Passacantando, S. Santucci, G. Czempik, J. Szuber, XPS study of the surface chemistry of L-CVD SnO_2 thin films after oxidation, Thin Solid Films 490 (2005) 36–42.
[53] M. Kwoka, G. Czempik, J. Szuber, X-ray photoemission spectroscopy study of the surface chemistry of laser-assisted chemical vapour deposition SnO_x thin films after exposure to hydrogen, Acta Phys. Slovaca 55 (2005) 331–339.
[54] S. Shukla, S. Seal, J. Akesson, R. Oder, R. Carter, Z. Rahman, Study of mechanism of electroless copper coating of fly-ash cenosphere particles, Appl. Suft. Sci. 181 (2001) 35–50.
[55] N. Faradzhev, V. Sidorkin, Hydrogen mediated transport of Sn to Ru film surface, J. Vac. Sci. Technol. A 27 (2009) 306–314.
[56] A.-M. Ungureanu, O. Oprea, B.S. Vasile, C. Andronescu, G. Voicu, I. Jitaru, Temperature effect over structure and photochemical properties of nanostructured SnO_2 powders, Cent. Eur. J. Chem. 12 (2014) 909–917.
[57] A. Katoch, J.H. Kim, Y.J. Kwon, H.W. Kim, S.S. Kim, Bifunctional sensing mechanism of SnO_2-ZnO composite nanofibers for drastically enhancing the sensing behavior in H_2 gas, ACS Appl. Mater. Interfaces 7 (2015) 11351–11358.
[58] S.H. Yan, S.Y. Ma, W.Q. Li, X.L. Xu, L. Cheng, H.S. Song, X.Y. Liang, Synthesis of SnO_2-heterostructured nanofibers for enhanced ethanol gas-sensing performance, Sens. Actuators B 221 (2015) 88–95.
[59] S.K. Misra, N.K. Pandey, Analysis on activation energy and humidity sensing application of nanostructured SnO_2-doped ZnO material, Sens. Actuators A 249 (2016) 8–14.
[60] L.F. da Silva, J.C. M'Peko, A.C. Catto, S. Bernardini, V.R. Masterlaro, K. Aguir, C. Ribeiro, E. Longo, UV-enhanced ozone gas sensing response of ZnO-SnO_2 heterojunctions at room temperature, Sens. Actuators B 240 (2017) 573–579.
[61] B.G. Ghule, S. Shaikh, S.U. Ekar, U.T. Nakate, K.C. Gunturu, N.M. Shnde, M. Naushad, K.H. Kim, C. O'Dwyer, R.S. Mane, Natural carbonized sugar as a low-temperature ammonia sensor material: experimental, theoretical, and computational studies, ACS Appl. Mater. Interfaces 9 (2017) 43051–43060.